IEEE Access
Multidisciplinary | Rapid Review | Open Access Journal

Received 13 June 2024, accepted 29 July 2024, date of publication 6 August 2024, date of current version 13 September 2024.

Digital Object Identifier 10.1109/ACCESS.2024.3439345

RESEARCH ARTICLE

Electromagnetic Radiation Leakage Imaging Localization on the Spacecraft Surface

YUTING ZHANG[1], (Member, IEEE), SHUANGHONG ZHOU[2], AND MIAO XIAO[1]
[1]Beijing Institute of Spacecraft System Engineering, Beijing 100094, China
[2]College of Mathematical Sciences, Harbin Engineering University, Harbin, Heilongjiang 150001, China

Corresponding author: Yuting Zhang (zhang_sch@163.com)

This work was supported in part by the National Natural Science Foundation of China under Grant 62201035.

ABSTRACT The localization of electromagnetic radiation leakage through cabin gaps is a critical and challenging aspect of electromagnetic compatibility design for spacecraft. This paper proposes a localization method based on synthetic aperture interferometric passive radiometry imaging. Electromagnetic radiation signals are measured at a certain distance from the spacecraft surface to form visibility samples. These visibility samples and the modified brightness temperature of the spacecraft surface electromagnetic radiation leakage constitute a pair for Fourier transform. The electromagnetic leakage location image of spacecraft surface is obtained through inverse Fourier transform. A sparse sampling method based on particle swarm optimization is proposed to improve testing efficiency. The impacts of various factors, including positional parameters, positioning accuracy of the test antenna, and scanning parameters on the imaging results are analyzed. Experiments are conducted on a cabin with 1 m×1 m×1 m having 51 holes on one surface. The algorithm proposed in this article is validated to effectively image and locate electromagnetic leakage points at different frequencies, with an absolute positioning error not exceeding 16mm. In addition, the effectiveness of the sparse sampling method is confirmed. Hence, it can accurately locate the position of electromagnetic leakage by saving 83.3% of the test time, with a misjudgment rate of 5.9%.

INDEX TERMS Radiometer imaging, electromagnetic interference localization, sparse sampling, particle swarm optimization, spacecraft.

I. INTRODUCTION

With the continuous advancement of space technology, the application of various complex payloads is increasingly extensive, leading to a more complex electromagnetic environment for spacecraft [1]. Against this backdrop, electromagnetic compatibility (EMC) design has become a crucial component in the development process of spacecraft [2]. For spacecraft with complex electromagnetic environments, improving the shielding effectiveness of the cabin panels is very important in the EMC design of spacecraft [3], [4]. For example, by improving the shielding effectiveness of the cabin panels, it is possible to prevent electromagnetic radiation from equipment inside the cabin from interfering with external sensitive systems, as well as to avoid interference to sensitive equipment inside the cabin from high-power radio frequency radiation outside.

However, in the actual design and manufacturing process, there are inevitably many gaps in the spacecraft cabin panels, which cause serious electromagnetic leakage. To enhance the shielding effectiveness of the cabin panels, precise localization and processing of these gaps are essential. Traditional methods, such as near-field probe sniff [5], [6], are not only limited in accuracy but also prone to missing holes that can cause electromagnetic leakage. For example, when the spacecraft surface is coated with thermal control layers, it is difficult to directly discover the holes hidden beneath the layers. Moreover, this method requires testing personnel to operate near the spacecraft, and for safety reasons, high-power radiation equipment on the spacecraft cannot be activated during this time. Because the testing environment is inconsistent with the actual in-orbit state, and the electromagnetic leakage locations measured may not match the

The associate editor coordinating the review of this manuscript and approving it for publication was Mohamed Kheir.

actual situation. Furthermore, the characteristics of electromagnetic leakage through different gaps vary at different frequencies, and some gaps with low radiation efficiency at certain frequencies may not require shielding. Therefore, it is necessary to locate electromagnetic leaks at specific EMC focus frequencies to prevent unnecessary shielding that leads to over-design in EMC. If there are many frequencies of interest, the efficiency of localization using near-field probes will be particularly low, and actual spacecraft often involve many sensitive frequencies, such as L-band navigation, S-band telemetry and control, C-band transponders, and so on.

Currently, the two more common methods for electromagnetic interference localization include near-field scanning [7], [8] and the use of electric/magnetic dipole equivalents [9], [10]. These methods mainly test the electric or magnetic field radiation characteristics of the object through near-field scanning and then use a dipole model to equivalently represent the object's electromagnetic radiation characteristics. The source of interference is then located by calculating dipole parameters based on the scanning results [11], [12]. Several improved methods have been derived on this basis. For example, an adaptive sampling method was proposed in [13]. The joint regularization method and dynamic differential evolution algorithm were used to address nonlinear problems in [14] and [15]. In the above studies, the dipoles are usually of the same form, so [16] used machine learning methods to reconstruct dipoles of different forms to further enhance the precision of analysis.

Moreover, several studies have explored the localization of interference sources located within shielded enclosures [17], such as the phase inversion method [18], the numerical Green functions method [19], [20] and so on. For spacecraft EMC design, effectively solving the problem of system electromagnetic interference can be achieved by locating electromagnetic leakages on the cabin panels, eliminating the need to locate internal interference sources, which is crucial for the accurate prediction of electromagnetic emission spectra.

It is worth noting that the aforementioned near-field scanning localization methods are mainly applied to smaller-sized scenarios, such as printed circuit boards (PCBs). When the object under test is large, such as a spacecraft structure cabin panel, the method will take a significant amount of time. Additionally, near-field scanning requires a scanning test plane to be sufficiently close to the object under test, but equipment on the surface of the spacecraft structure may prevent the creation of a complete and close test plane, which somewhat restricts the application of near-field scanning methods for locating electromagnetic radiation leaks on spacecraft cabin panels. In [21], the localization of interference sources was conducted based on the principles of synthetic aperture radar. But this method is more effective for far-field radiation. For spacecraft, it is rather difficult to meet far-field conditions due to the multiplicity of EMC design focus frequencies. In [22], eigenmode currents and Fourier transforms were used for interference source localization, This method requires a certain distribution of current, making it less suitable for cases of gap leakage. Time reversal-based techniques for reconstructing radiation interference sources were also proposed in [23]. However, these methods are primarily suitable for PCB-level interference source localization.

In this paper, a positioning method based on synthetic aperture interferometric passive radiometer imaging is proposed. This method addresses the problem of electromagnetic radiation leakage which is usually caused by spacecraft cabin panels. We measure the electric field radiation at a certain distance, and then we can invert and locate the electromagnetic leakage point on the cabin panel. Further, we analyze the principle of this imaging localization and in accordance with the regulation requiring test antennas to be 1 meter away from the spacecraft during electromagnetic radiation emission testing. Meanwhile, we perform the near-field correction based on the phase of the visibility sample function. Simulation analysis is performed on the testing parameters and testing errors that affect imaging quality, which includes the positional parameters, test antenna position accuracy and scanning parameters. In order to improve testing efficiency in actual processes, we research a sparse sampling method based on the particle swarm optimization algorithm and analyzed the impact of different sparse sampling methods on imaging localization results. In the fifth section of the paper, experiments verification ensures that the algorithm studied in this paper can effectively locate the holes causing electromagnetic radiation leakage on spacecraft cabin panels. It can also locate the main holes causing electromagnetic radiation leakage at different frequencies. At the same time, the effectiveness of the sparse sampling method is also proven, as it can significantly reduce the testing time while maintaining accuracy in localization.

II. ELECTROMAGNETIC RADIATION LEAKAGE LOCALIZATION BASED ON SYNTHETIC APERTURE INTERFEROMETRY PASSIVE RADIOMETER IMAGING

A. IMAGING AND LOCALIZATION PRINCIPLE

The principle of electromagnetic radiation leakage localization based on synthetic aperture interferometry passive radiometer imaging is shown in Fig. 1. The spacecraft surface that generates electromagnetic leakage is the target plane. The antenna is used to measure electromagnetic leakage signals at a certain distance from the target plane. The measurement range of the antenna is a plane, which is the antenna scanning plane. The signals obtained from scanning measurements form a visibility sample space. By processing data in the visibility sample space, imaging of the electromagnetic leakage plane of the spacecraft surface can be obtained. The spacecraft surface adopts a Cartesian coordinate system (x,y). The antenna scanning plane is represented using directional cosine (ξ, η). And (u,v) coordinates is used to represent in visibility sample space.

At a certain distance from the surface of the spacecraft, an antenna scans and tests the electromagnetic radiation

signal. For each scanning test position, the antenna receives the electromagnetic radiation signal from the surface of the spacecraft, which can be represented as:

$$\chi_i(t) = \sum_s \frac{\alpha(\xi,\eta)\,[\Delta s(\xi,\eta)]^{1/2}}{r_i(\xi,\eta)} \exp\left(-j\frac{2\pi}{\lambda} r_i(\xi,\eta)\right) \tag{1}$$

where (ξ, η) represents the direction cosines of each point on the target aperture to the center point of the antenna scanning plane. $\xi = \sin\theta\cos\varphi$. $\eta = \sin\theta\sin\varphi$. $\Delta s(\xi, \eta)$ represents the discretized micro-area on the target plane corresponding to $\alpha(\xi, \eta)[\Delta s(\xi, \eta)]^{1/2}$ which characterizes the radiation signal strength generated on the micro-area $\Delta s(\xi, \eta)$. $\alpha(\xi, \eta)$ can be regarded as the radiation signal strength generated per unit area within $\Delta s(\xi, \eta)$. $r_i(\xi, \eta)$ is the distance from the micro-area $\Delta s(\xi, \eta)$ to the test antenna. λ is the wavelength. The target plane refers to the surface of a spacecraft that generates electromagnetic radiation leakage.

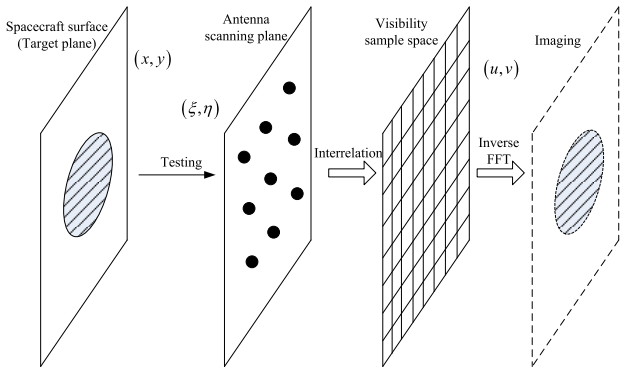

FIGURE 1. Imaging and localization principle.

The received signals from two test antennas at any positions i and j are cross-correlated:

$$\begin{aligned} &E\{\chi_i(t)\chi_j^*(t)\} \\ &= E\left\{\left[\sum_s \frac{\alpha(\xi,\eta)\,[\Delta s(\xi,\eta)]^{1/2}}{r_i(\xi,\eta)} \exp\left(-j\frac{2\pi}{\lambda} r_i(\xi,\eta)\right)\right]\right. \\ &\left.\times\left[\sum_s \frac{\alpha(\xi,\eta)\,[\Delta s(\xi,\eta)]^{1/2}}{r_j(\xi,\eta)} \exp\left(j\frac{2\pi}{\lambda} r_j(\xi,\eta)\right)\right]\right\} \end{aligned} \tag{2}$$

Since the radiation signals from different micro-areas $\Delta s(\xi, \eta)$ are uncorrelated with each other, (2) can be rewritten as:

$$\begin{aligned} &E\{\chi_i(t)\chi_j^*(t)\} \\ &= E\left\{\sum_s \frac{\alpha^2(\xi,\eta)\Delta s(\xi,\eta)}{r_i(\xi,\eta) r_j(\xi,\eta)} \exp\left(j\frac{2\pi}{\lambda}[r_j(\xi,\eta) - r_i(\xi,\eta)]\right)\right\} \\ &= \sum_s \frac{E\{\alpha^2(\xi,\eta)\}}{r_i(\xi,\eta) r_j(\xi,\eta)} \exp\left(j\frac{2\pi}{\lambda}[r_j(\xi,\eta) - r_i(\xi,\eta)]\right) \\ &\quad \Delta s(\xi,\eta) \end{aligned} \tag{3}$$

where $\alpha^2(\xi, \eta)$ is the square radiation signal strength generated per unit area within $\Delta s(\xi, \eta)$.

As shown of the surface microelement Δs in Fig. 2, the microelement position in a Cartesian coordinate system is X_0, Y_0 and Z_0. When the receiving antennas are at positions i and j, the distance between the antennas and microelement is r_i and r_j, respectively. Then a Taylor approximation for r_i and r_j can be obtained:

$$\begin{aligned} r_{i\,\mathrm{or}\,j}(\xi,\eta) &= \sqrt{(X_0 - x_{i\,\mathrm{or}\,j})^2 + (Y_0 - y_{i\,\mathrm{or}\,j})^2 + Z_0^2} \\ &= \sqrt{r^2(\xi,\eta) + d_{i\,\mathrm{or}\,j}^2 - 2(X_0 x_{i\,\mathrm{or}\,j} + Y_0 y_{i\,\mathrm{or}\,j})} \\ &\approx r(\xi,\eta) + \frac{d_{i\,\mathrm{or}\,j}^2 - 2(X_0 x_{i\,\mathrm{or}\,j} + Y_0 y_{i\,\mathrm{or}\,j})}{2r(\xi,\eta)} \\ &= r(\xi,\eta) + \frac{d_{i\,\mathrm{or}\,j}^2}{2r(\xi,\eta)} - \xi x_{i\,\mathrm{or}\,j} - \eta y_{i\,\mathrm{or}\,j} \end{aligned} \tag{4}$$

where x and y represent antenna position in the coordinate system. d represents the distance between the antenna and the coordinate origin.

Thus:

$$r_i(\xi,\eta) - r_j(\xi,\eta) = \frac{d_i^2 - d_j^2}{2r(\xi,\eta)} - \xi(x_i - x_j) - \eta(y_i - y_j) \tag{5}$$

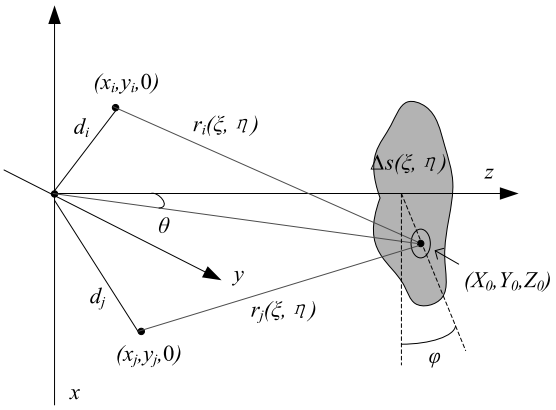

FIGURE 2. Positional relationship.

If the distance between the surface of the spacecraft and the test antenna plane is larger (i.e., $d \gg d_{i,j}$), then:

$$r_i(\xi,\eta) - r_j(\xi,\eta) \approx -\xi(x_i - x_j) - \eta(y_i - y_j) \tag{6}$$

Additionally, the micro-area $\Delta s(\xi, \eta)$ can be expressed using $\Delta\xi$, $\Delta\eta$:

$$\Delta s(\xi,\eta) = \frac{r^2(\xi,\eta)}{\cos\theta}\Delta\xi\,\Delta\eta \tag{7}$$

The above equations can be combined:

$$\begin{aligned} &E\{\chi_i(t)\chi_j^*(t)\} \\ &= \sum_s \frac{E\left[\alpha^2(\xi,\eta)\right]}{\cos\theta} \\ &\quad \cdot \exp\left(-j2\pi(\xi\frac{x_i - x_j}{\lambda} + \eta\frac{y_i - y_j}{\lambda})\right)\Delta\xi\,\Delta\eta \end{aligned} \tag{8}$$

$E[\alpha^2(\xi,\eta)]$ reflects the relative radiation capability at each position (ξ, η) on the target aperture, which is proportional to the brightness temperature at each position [24]. $T(\xi,\eta)$ can be regarded as a correction to $E[\alpha^2(\xi,\eta)]$, called the corrected brightness temperature, denoted as $T(\xi,\eta) = E[\alpha^2(\xi,\eta)]/\cos\theta$. By setting $u = (x_i\text{-}x_j)/\lambda$ and $v = (y_i\text{-}y_j)/\lambda$, $T(\xi,\eta)$ and the visibility function $V(u,v)$ can be transformed into a Fourier pair.

$$V(u,v) = \iint T(\xi,\eta)\exp\left(-j2\pi(\xi u+\eta v)\right)d\xi d\eta \tag{9}$$

When enough sample values of the visibility function $V(u,v)$ are obtained through testing, the distribution of the target's corrected brightness temperature $T(\xi,\eta)$ can be obtained using the inverse Fourier transform:

$$\begin{aligned} T(\xi,\eta) &= F^{-1}\left[V(u,v)\right] \\ &= \frac{1}{2\pi}\iint V(u,v)\exp\left(j2\pi\left(u\xi+v\eta\right)\right)du\,dv \end{aligned} \tag{10}$$

The electromagnetic radiation leakage on the surface of the spacecraft can be located by obtaining the corrected brightness temperature of the target, i.e., the electromagnetic radiation intensity on the surface of the spacecraft.

B. NEAR FIELD CORRECTION

The above analysis was derived under far-field conditions. However, for spacecraft electromagnetic radiation testing, far-field conditions may not always be met, and many situations belong to near-field conditions. In this case, since the right side of (5) cannot be ignored, the direct relationship between the visibility sample function $V(u,v)$ obtained by measurement and the Fourier transform of the corrected brightness temperature $T(\xi,\eta)$ no longer holds. Therefore, the point source correction method is used to correct the phase of the visibility sample function $V(u,v)$.

If we assume that a point source is constructed at the position on the spacecraft surface in Fig. 3, with the direction cosine coordinates (ξ_0,η_0). The visibility sample function $V_p(u,v,\xi_0,\eta_0)$ of the point source obtained by measurement can be approximated at each sampling point (u,v) as:

$$V_p(u,v) = V(u,v)\exp\left(-jP^*(u,v,\xi_0,\eta_0)\right) \tag{11}$$

where P^* is the corrected phase. Since $P(u,v,\xi_0,\eta_0)$ can be obtained by measurement, and $(\xi_0 u+\eta_0 v)$ is known, the phase that needs to be corrected for the visibility sample function $V(u,v)$ at the target position (ξ_0,η_0) when imaging the electromagnetic leakage on the surface of the spacecraft is:

$$\begin{aligned} P^*(u,v,\xi_0,\eta_0) &= 2\pi\frac{d_i^2-d_j^2}{2r(\xi,\eta)\lambda} \\ &= P(u,v,\xi_0,\eta_0)+2\pi(\xi_0 u+\eta_0 v) \end{aligned} \tag{12}$$

P is the phase at the test position defined as:

$$P(u,v,\xi_0,\eta_0) \approx 2\pi\left[\frac{d_i^2-d_j^2}{2r(\xi,\eta)\lambda}-(\xi_0 u+\eta_0 v)\right] \tag{13}$$

In Fig. 3, it is assumed that the electromagnetic leakage source point is (ξ_0,η_0). Due to the fact that a hole has a certain area. So in practical applications, it is necessary to process the effective correction aera (ξ,η). Since the phase value $P^*(u,v,\xi,\eta)$ that needs to be corrected for $V(u,v)$ is similar to $P^*(u,v,\xi_0,\eta_0)$ within the range near the point source (ξ_0,η_0) shown in Fig. 3. This correction is effective in the vicinity of (ξ_0,η_0). That is, the $T^*(\xi,\eta)$ obtained by inversion through (14) matches the corrected brightness temperature $T^*(\xi,\eta)$ in the range near (ξ_0,η_0).

$$\begin{aligned} T^*(\xi,\eta) &= F^{-1}\left[V_p(u,v)\right] \\ &= \frac{1}{2\pi}\iint V_p(u,v)\exp\left(j2\pi\left(u\xi+v\eta\right)\right)du\,dv \end{aligned} \tag{14}$$

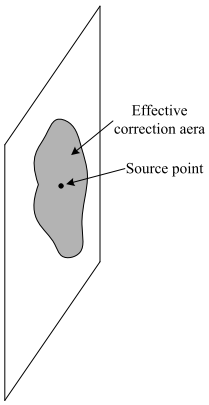

FIGURE 3. Near field correction.

C. IMAGING QUALITY

The accuracy of locating radiative interference is determined by the quality of the imaging, and the imaging quality is related to the parameters of the near-field scanning test. The most important parameter in assessing imaging quality is the resolution, and the relationship between the resolution and the scanning parameters can be derived from the near-field spatial spectrum. The field distribution on the plane satisfies the Fourier transform relationship with the spatial spectrum [25]:

$$\begin{aligned} E(x,y,z) = &\int_{-\infty}^{+\hbar}\int_{-\infty}^{+\infty} F\left(k_x,k_y\right)\exp\left(-jk_z z\right) \\ &\cdot\exp\left(-j\left(k_x x+k_y y\right)\right)dx\,dy \end{aligned} \tag{15}$$

where $F(k_x,k_y)$ is the spatial spectrum. k is the wave constant in free space. k_x, k_y, k_z are the three components of k.

The electric field distribution $E(x,y,z)$ on the plane and the spatial spectrum $F(k_x,k_y)$ satisfy the Fourier transform relationship. Therefore, the resolutions dk_x and dk_y of k_x and k_y are related to the scanning range D_x and D_y as follows:

$$\begin{cases} dk_x = 2\pi/D_x \\ dk_y = 2\pi/D_y \end{cases} \tag{16}$$

The angular resolution $d\theta$ can be derived from dk_x and dk_y:

$$\begin{cases} dk_x = k\cos\theta\cos\varphi d\theta - k\sin\theta\sin\varphi d\varphi \\ dk_y = k\cos\theta\sin\varphi d\theta - k\sin\theta\cos\varphi d\varphi \end{cases} \tag{17}$$

$$d\theta = \frac{\cos\varphi dk_x + \sin\varphi dk_x}{k\cos\theta} \tag{18}$$

If we assume $D_x = D_y = D$, the magnitude expression for the angular resolution can be written as:

$$d\theta = \frac{\lambda}{D\cos\theta} \tag{19}$$

Therefore, the imaging resolution dl is:

$$dl = \frac{\lambda z}{D\cos\theta} \tag{20}$$

where z is the distance from the antenna test plane to the spacecraft surface. D is the range of the scanning plane, and θ is the angle between the line connecting the imaging point to the scanning center and the z-axis shown in Fig. 2. From (20), it is known that to obtain an accurate image of the leakage point, we can increase the scanning range and shorten the distance between the scanning plane and the test object.

III. SPARSE SAMPLING

In the process of antenna sampling, if the time cost is higher than the hardware cost, then it is necessary to optimize the sampling array, in order to obtain satisfactory imaging localization results through sparse sampling. For the optimization of the sampling array, the basic principle is to achieve a "best" balance among various parameters of the imaging system (mainly referring to spatial resolution, imaging range, etc.) under the premise of obtaining a certain imaging quality, taking into account the constraints between the parameters. The final image of the leakage points is a composite result of all the sampling points. The lack of individual sampling points can still generate an image, but the quality of the imaging results will decline. However, some data plays a major role in the result, while the absence of other sampling points has little impact on the imaging quality, which can lead to resource waste and increase the difficulty of system implementation. To minimize redundancy while not reducing imaging quality, it is necessary to arrange the sampling points in reasonable positions.

However, in actual systems, since the physical aperture of the actual antenna cannot be very small, sparse array arrangements need to be used to avoid aliasing. Moreover, during the array arrangement, in order to use the Fourier transform algorithm with faster computing speed in the inversion algorithm, it is necessary to place the sampling points on regular cells. At the same time, a specific algorithm must be used to minimize the redundancy of sampling points to avoid aliasing during image inversion. Hence, provide images of the same quality with fewer sampling points.

At this point, optimization of the antenna sampling positions is needed. This paper adopts the particle swarm optimization algorithm for optimization. In antenna sampling position optimization, the most important thing is to establish an optimization objective function. The purpose of optimizing the sampling point positions is to make the visibility sampling points formed by the antenna array as uniformly distributed as possible in a certain area under necessary constraints. For any antenna distribution in an arbitrary area, the mathematical description of the minimum distance product objective function is as follows. Assume there are N sampling points in an arbitrary area Ω, with their positions represented as $r_1, r_2, \ldots, r_N$, $r_i \in \Omega$, $i = 1, 2 \ldots, N$. For any two points i and j, their baseline is $\rho_{ij} = r_i\text{-}r_j$. Let the nearest sampling distance between any two points be d, that is, $d = \min\{|r_i\text{-}r_j|\}$ $(r_i \neq r_j)$. Then the minimum distance objective function formed by the position variables of these N sampling points is

$$\begin{cases} f(r_1, r_2, \ldots, r_N) = -\sum_{i,j,k,l} \lg(|\rho_{ij} - \rho_{kl}|) \\ r_i \in \Omega, i = 1, 2, \ldots N \\ \min\{|r_i - r_j|\} \geq d, i \neq j \end{cases} \tag{21}$$

Further explanation of the above objective function is as follows. The optimization goal is to calculate $\min[f(r_1, r_2, \ldots, r_N)]$. When any two visibility sampling points are very close, i.e., $|\rho_{ij} - \rho_{kl}| \to 0$, it is equivalent to these two visibility sampling points becoming redundant, which is an undesirable situation in antenna surface. At this time, the objective function will add a large positive term, i.e., $-\lg(|\rho_{ij}-\rho_{kl}|) \to +\infty$. However, the optimization process aims to minimize the objective function, so situations where redundancy increases the objective function are gradually discarded during optimization. Therefore, this objective function is reasonable in eliminating visibility redundancy or preventing visibility sampling points from being too close. Additionally, the objective function uses a logarithmic form to convert multiplicative operations into additive operations because the logarithmic function is monotonically increasing in the positive real number domain, so this transformation does not change the monotonicity of the objective function. The main purpose of the logarithmic transformation is to avoid overflow when the number of antennas is large, as multiplication may lead to overflow, while addition can avoid it.

The calculation process for optimizing the antenna sampling positions using the particle swarm optimization algorithm is shown in Table 1.

A simulation analysis is conducted for sparse sampling. The simulation model consists of a 1.2 m by 1.2 m panel with 4×4 uniformly distributed holes. Electromagnetic radiation leakage signal collection is performed 1 meter away from the panel, with a collection range of 1 m$\times$1 m. The analysis frequency is 12 GHz. The left image in Fig. 4 shows the signal collection results, and the right image shows the imaging results without sparse sampling. It can be seen from the figure that electromagnetic radiation leakage imaging can effectively locate the leaking holes.

Imaging was performed using "+" and "Y" sampling type. After processing with the optimization algorithm

TABLE 1. Optimization process of particle swarm algorithm.

Step	Process
1	Initialization. This includes setting the velocity and position of the particles, learning factors, inertia weight, termination conditions, etc. The particle position range can be set to the test's maximum boundary. The learning factor can be set to 1.5, and the inertia weight can be set between 0.35 and 0.85.
2	Calculate the best position and value for each individual particle, as well as the global best position and value for the swarm.
3	Update the position and velocity values. Determine whether to replace the individual particle's best position and value, and the swarm's global best position and value.
4	Determine whether the termination conditions are met. If so, end the optimization process and output the optimized values; if not, continue with iterative optimization.
5	Test the design of the objective function and the selection of initial parameters set previously, mainly to see whether the convergence curve has stabilized, whether the results of several optimizations are roughly the same, and whether the results of the optimization reflect the actual optimization problem accurately.

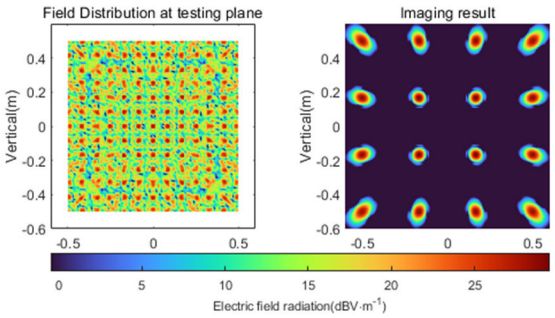

FIGURE 4. Signal collection and imaging localization results without sparse sampling.

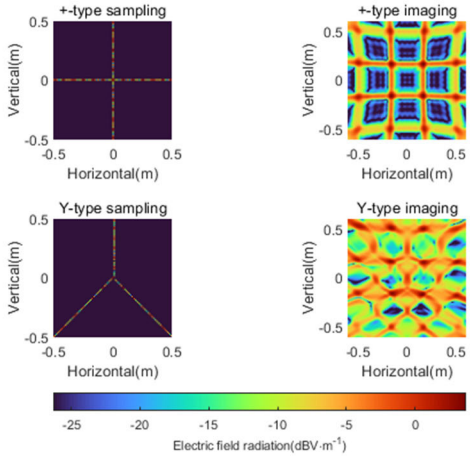

FIGURE 5. Imaging localization results of sparse sampling array.

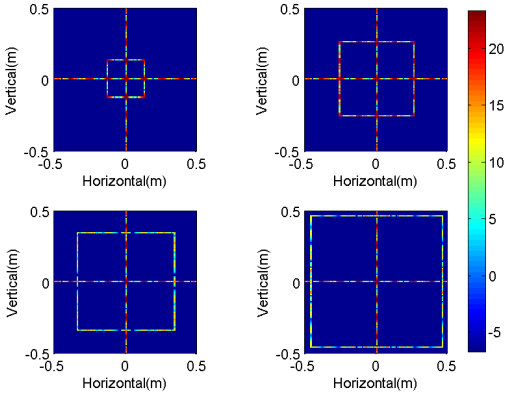

FIGURE 6. "⋕"sampling type.

described in this section, the sampling array pattern and imaging results are shown in Fig. 5. The "+" sampling type reduced the number of sampling points by 80.3%, while the "Y" sampling type reduced the number of sampling points by 85.3%.

From the analysis results, it is evident that it is still possible to locate the holes leaking electromagnetic radiation after sparse sampling. Comparatively, the "+" type sampling provides better imaging effects. Although the "Y" type sampling can also locate the holes, there is a certain degree of signal overlap in the imaging results, making the localization effect less clear than that of the "+" type sampling. Due to the relatively regular arrangement of holes here, the "+" sample type is relatively consistent with the arrangement of holes, which can collect more electromagnetic leakage signals. So the localization effect is relatively better. Furthermore, a model with 5×5 distributed holes was analyzed. The sampling type was "⋕" shown in Fig. 6.

The imaging results are shown in Fig. 7. We adjusted the position of the sampling midpoints type, and the imaging effect also changes according. When the middle "□" type is small, the electromagnetic leakage signals from the peripheral holes cannot be collect. So the localization effect is not good. When the "□" type is large enough to obtain more electromagnetic leakage signals, it can effectively locate the electromagnetic leakage points. Therefore, the sparse sampling type should cover as many electromagnetic leakage points as possible.

When the sampling type is selected, it is advisable to use a form similar to the distribution of holes as much as possible. In the analysis of this paper, due to the distribution of holes being arranged in a rectangular array, so the "+" type sparse sampling method can be adopted in applications.

IV. IMAGING PARAMETER ANALYSIS

A. ANALYSIS MODEL

This section focuses on analyzing the parameters that affect imaging localization. The analysis model is a spacecraft cabin with dimensions 2 m×2 m×2 m, with holes uniformly distributed within a range of ±0.5 m from the center on one of its faces, as shown in Fig. 8. The analysis frequency is 12 GHz.

B. INFLUENCE OF POSITIONAL PARAMETERS

Positional parameters include the distance between the antenna test surface and the spacecraft panel, and the inclination angle of the test surface. As shown in Fig. 9, the effect

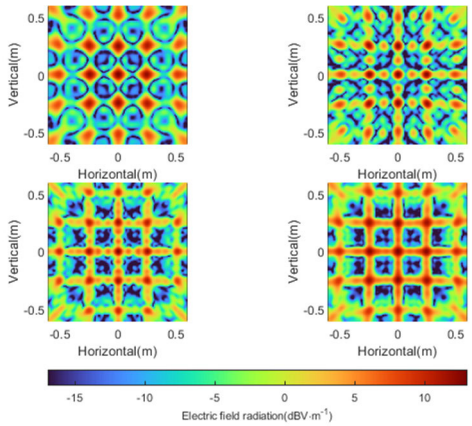

FIGURE 7. Imaging results with different "⌖" sampling type.

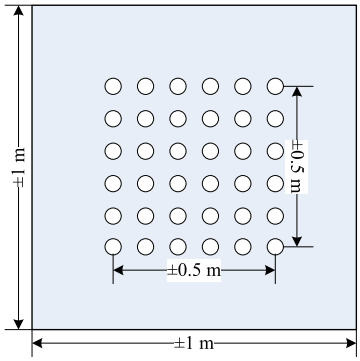

FIGURE 8. Imaging parameter analysis model.

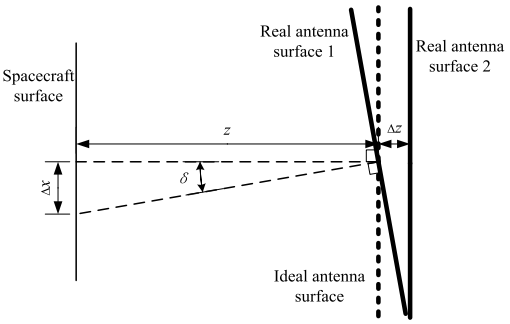

FIGURE 9. Schematic of positional parameter deviations.

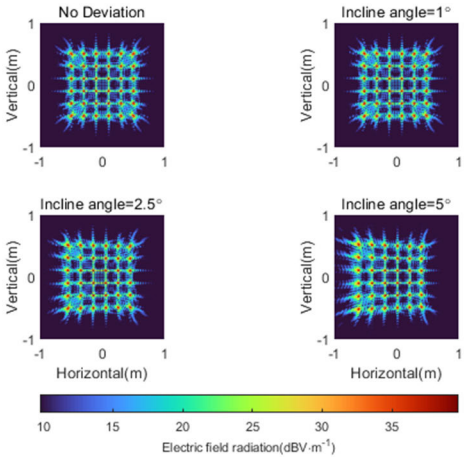

FIGURE 10. Analysis of the influence of inclination angle on imaging localization.

of distance deviation and angle deviation on the imaging location deviation can be derived from the geometric relationship of the positions. Assuming z is the distance between the panel and the antenna test surface, Δz is the distance error. The ideal antenna test surface should be parallel to the spacecraft surface, with δ being the inclination angle. x is the actual position of the electromagnetic interference leakage, and Δx is the imaging localization position deviation. The relationship between the imaging localization error and the test distance deviation and angle deviation is as follows:

$$\begin{cases} x = z \tan \delta \\ \Delta x = x \Delta z / z \end{cases} \tag{22}$$

In Fig. 10, the cases with inclination angles of 1°, 2.5°, and 3° are analyzed. The average positioning errors are 7.8 mm, 14.5 mm, and 26.2 mm, respectively. If the average positioning error is required to not exceed 20 mm, then the analysis shows that when the inclination angle error is within 2.5°, the imaging localization accuracy can meet application requirements.

In Fig. 11, the cases with distance errors of -15 cm, 10 cm, and 15 cm are analyzed. The average positioning range error is 12 cm, 3.8 cm, and 10 cm, respectively. If the average positioning range error is required to not exceed 4 cm, then the analysis cases indicates that when the distance error is within 10 cm, the imaging localization accuracy can meet application requirements.

If we compare the analysis results from Figs. 10 and 11, it can be conclude that the positional parameters not only affect the localization position but also reduce the beam-focusing effect of the electromagnetic radiation leakage points. In practical applications, it is necessary to ensure the precision of the antenna scanning position and to ensure that it is parallel to the test spacecraft panel.

C. INFLUENCE OF TEST ANTENNA POSITIONING ACCURACY

The positioning accuracy of the test antenna will also affect the precision of imaging localization. As the antenna position is represented in three-dimensional space, deviations can occur in the x, y, and z directions. The resulting image with positioning errors can be expressed as the product of the true position image and an error image, as shown in (23):

$$\begin{aligned} E'\left(x', y'\right) = \sum_{n=1}^{N} \sum_{m=1}^{M} & \left[E\left(x_n, y_m\right)\right. \\ & \cdot \exp\left[jk\left(x_n + \Delta x\left(x_n, y_m\right) - x'\right)^2\right. \\ & + \left(y_m + \Delta y\left(x_n, y_m\right) - y'\right)^2 \\ & \left.\left. + \left(z + \Delta z\left(x_n, y_m\right)\right)^2\right]\right] \end{aligned} \tag{23}$$

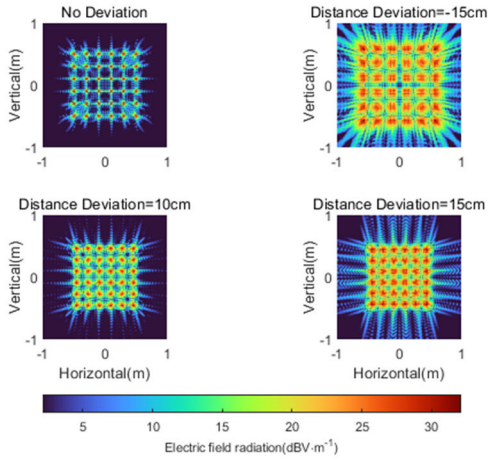

FIGURE 11. Analysis of the influence of distance error on imaging localization.

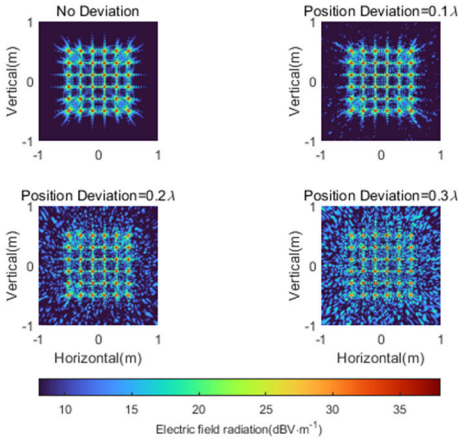

FIGURE 12. Analysis of lateral positioning error of test antenna on imaging localization.

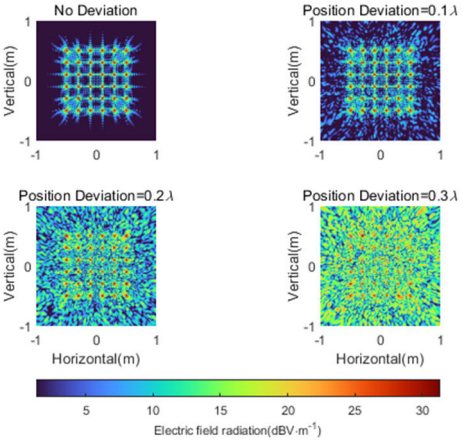

FIGURE 13. Analysis of longitudinal positioning error of test antenna on imaging localization.

In (23), $\Delta x(x_n, y_m)$, $\Delta y(x_n, y_m)$ and $\Delta z(x_n, y_m)$ represent the errors of the test antenna in the x, y and z directions, respectively. The accuracy deviation of the antenna positioning ultimately leads to a phase deviation. Therefore, the positioning error can be converted into a phase error. The derivative of the phase part of the spatial transformation factor $\Delta\phi(x, y, z) = k(x^2 + y^2 + z^2)^{1/2}$ is given by

$$\begin{cases} \dfrac{\partial\phi}{\partial x} = \dfrac{2\pi}{\lambda} \dfrac{xdx}{\left(x^2+y^2+z^2\right)^{1/2}} \\ \dfrac{\partial\phi}{\partial y} = \dfrac{2\pi}{\lambda} \dfrac{ydy}{\left(x^2+y^2+z^2\right)^{1/2}} \\ \dfrac{\partial\phi}{\partial z} = \dfrac{2\pi}{\lambda} \dfrac{zdz}{\left(x^2+y^2+z^2\right)^{1/2}} \end{cases} \tag{24}$$

The influence of the antenna's z-direction positioning error is the same as the distance error discussed in the previous section. Due to the symmetry in the x and y directions, the positioning errors in these two directions are given separately as lateral and longitudinal positioning errors and are expressed as phase error impacts:

$$\begin{cases} \Delta\phi_h = \dfrac{2\pi}{\lambda} \dfrac{\Delta l_h}{\sqrt{1+\frac{2z}{D}}} \\ \Delta\phi_v = \dfrac{2\pi\,\Delta l_v}{\lambda} \end{cases} \tag{25}$$

where $\Delta\phi_h$ and $\Delta\phi_v$ represent the phase errors caused by the lateral positioning error Δl_h and longitudinal positioning error Δl_v, respectively. D is the scanning range.

Figs. 12 and 13 present the analysis results for antenna positioning errors of 0.1λ, 0.2λ, and 0.3λ. The analysis shows that the longitudinal positioning error has a more significant impact on imaging localization. The positioning error of the test antenna should be less than one-tenth of the testing wavelength to ensure positioning accuracy.

D. INFLUENCE OF SCANNING PARAMETERS

The primary scanning parameters include the distance z between the plane of the test antenna and the spacecraft panel, and the scanning range D of the test antenna. Fig. 14 shows the imaging localization analysis results for distances of 1m, 2 m, 3 m, and 5 m. From the analysis, it can be seen that as the distance increases, the resolution decreases. However, at a distance of 5 m, it is still possible to distinguish electromagnetic radiation leakage positions of 14 cm. Generally, EMC test standards specify that the distance for spacecraft electric field radiation testing is 1m [26], which provides good resolution at this distance.

Fig. 15 shows the results of the influence analysis of the scanning range. The scanning ranges are set to 0.5 m, 1 m, 2 m, and 3 m. The analysis indicates that a relatively good imaging localization result can be obtained if the scanning range is larger than the radiation aperture of the tested spacecraft panel.

If the test range is limited, only a small range of scanning can be performed. Or there is not a sufficiently large scanning device, the entire sampling range cannot be tested at once.

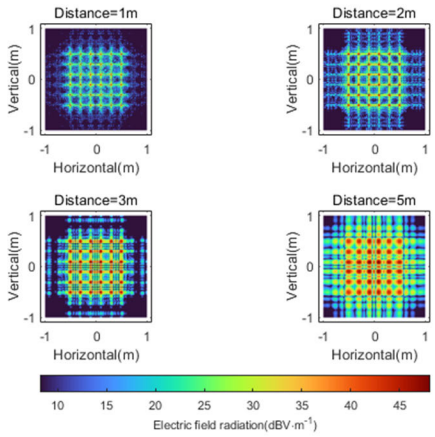

FIGURE 14. Analysis of the influence of test distance on imaging localization.

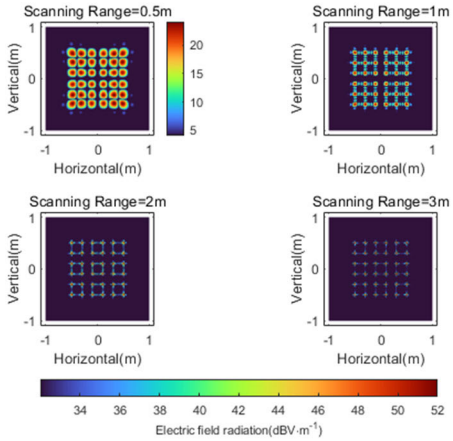

FIGURE 15. Analysis of the impact of scanning on imaging localization.

This may affect the imaging localization effect. In this case, a localized scanning method can be used, where different positions are scanned and imaged separately to achieve a relatively better resolution. Fig. 16 shows an example of partition scanning. There are two gaps on the cabin panel with a width of 5 mm and 2 mm, and a length of 150 mm and 212 mm, respectively. The excitation source is vertical polarization. The corresponding areas of these two gaps were scanned separately. The scanning and imaging results are shown in Fig.15. The left figures are the scanning results, while the right figure is the imaging result. Due to the stronger coupling effect of horizontal gap on vertical polarized waves, the electromagnetic radiation intensity at the horizontal gap is higher from the imaging result. From the analysis results, it can be seen that partition scanning can also achieve good positioning results. And the gaps can also be located. For the horizontal gap, the position with the strongest radiation is the position of the gap. For incline gap, although the imaging width is about 8 mm larger than the actual gap width, the centerline position of the gaps is accurate. The error of the centerline position is less than 0.7 mm. In practical application, there is still good support for the electromagnetic leakage localization.

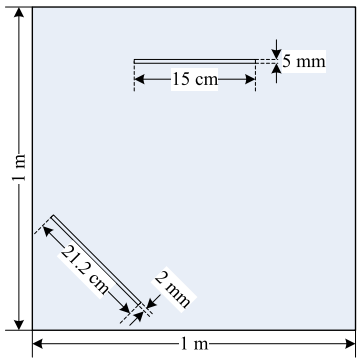

FIGURE 16. Partition scanning positioning model.

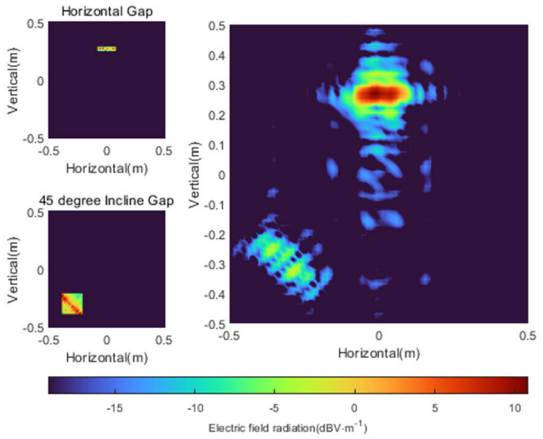

FIGURE 17. Partition scanning positioning result.

V. EXPERIMENTAL VERIFICATION

A. EXPERIMENTAL SCHEME

The experimental verification is conducted to validate the algorithm proposed in this paper. A 1 m×1 m×1 m cabin is designed with 51 holes on one of its surfaces. The diameter of the holes is 1 cm. An antenna scanning surface was set up 1 meter away from the holes. The test schematic is shown in Fig. 18, where an excitation antenna was placed inside the structure. During the testing process, the origin of the coordinate system was at the center of the cabin panel. The excitation antenna was placed at (0, 0, −0.6 m).The scanning antenna was mounted on a programmable scanning frame. Both the excitation and scanning antennas were connected to a vector network analyzer(VNA). The scanning frame adopts a two-dimensional scanning method, with a scanning range of 2 m × 2 m and a positioning accuracy of 0.05mm. The 6 GHz probe is WR-137. The 20 GHz probe is WR-42. The electromagnetic radiation leakage distribution on the antenna scanning test surface was obtained using the $S21$ parameter measured by the vector network analyzer. A photo of the testing site is shown in Fig. 19. The scanning range was 1m×1m.

B. EXPERIMENTAL RESULTS

For the aforementioned test setup, the localization of electromagnetic radiation leakage points was performed. Fig. 20

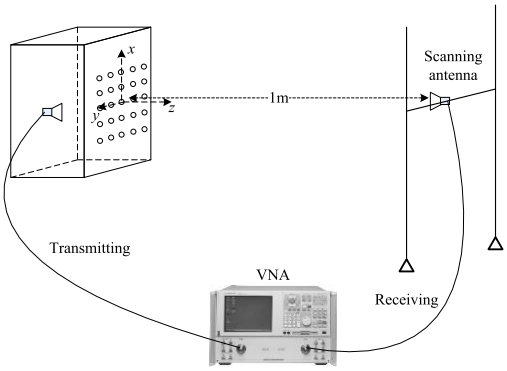

FIGURE 18. Test schematic.

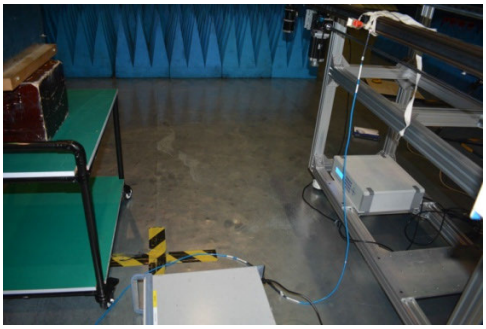

FIGURE 19. Test graph.

shows the imaging localization results at 6 GHz, with the actual holes positions marked by circles. In addition, we conducted simulation analysis using CST software. The analysis method adopts the Finite Integration Technique. The meshes were generated according to $\lambda/10$. Set the boundary condition to open (add space). This boundary condition is equivalent to a perfect matching layer, where electromagnetic waves pass almost without reflection. It can be used for situations equivalent to free space.

The simulation analysis and experimental results are basically consistent. From the imaging localization results, the majority of electromagnetic radiation leakage points were able to be located. For the presence of excitation in the cavity, the distribution of electromagnetic field is uneven. So the electromagnetic leakage intensity varies between different holes. When the holes are denser, the equivalent leakage hole area is larger, so the electromagnetic leakage of the left area is stronger that of the right. As shown in (19) and (20), the imaging localization resolution is related to frequency. When the frequency is low, the resolution decreases. So for 6 GHz, due to the relatively lower test frequency, some holes that are closer in distance are not effectively located.

At higher frequencies, the electric field radiation efficiency of the holes increased, and the imaging localization for each hole was essentially accurate. Fig. 22 shows the error curve of the localization point based on the maximum imaging radiation intensity compared to the actual hole positions. The results indicate that the positioning error is within a 16 mm range, which can meet practical application requirements.

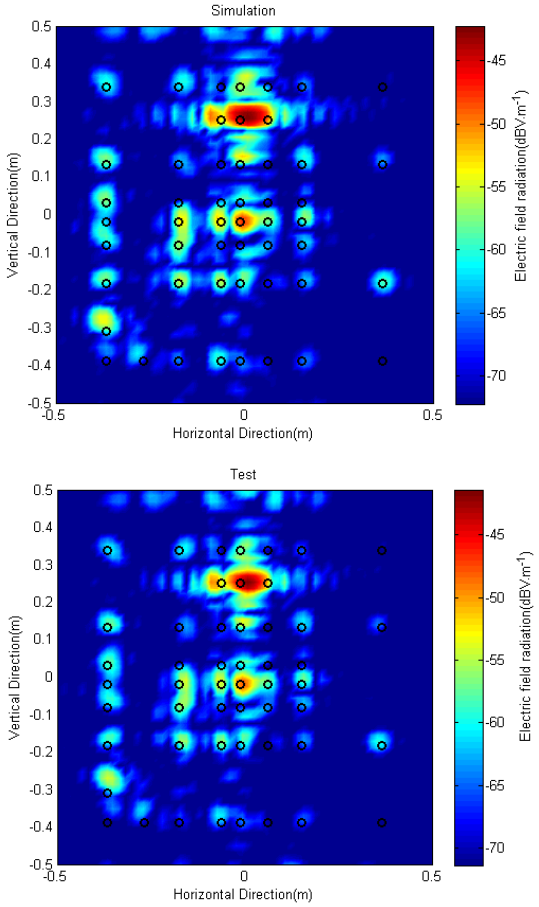

FIGURE 20. Imaging localization results at 6GHz.

The analysis results from Figs. 20 and 21 also show that at different frequencies, the positions of radiation from the panel vary. This proves that the method described in this paper can be used to locate electromagnetic radiation leakage points at frequencies of interest. In practical engineering applications, the imaging localization can be used to locate the holes with electromagnetic radiation, while avoiding over-design for electromagnetic compatibility.

The above process took about 90 minutes during the electric field radiation test. If there is significant time constraint, the sparse sampling method described in Section III can be used. After optimization with the particle swarm algorithm, a "+" type sampling method was performed. The imaging localization result under this sampling method is shown in Fig. 23.

The analysis results indicate that under sparse sampling conditions, effective imaging localization can still be performed for each electric field leakage point. As shown in the right image of Fig. 23, there are three misjudged leakage points (marked with blue triangle symbols). Although there are misjudged positions, the proportion is small at 5.9%. The test time in this case was about 15 minutes, saving approximately 83.3% of the time. The cost of misjudged positions relative to the time saved is acceptable.

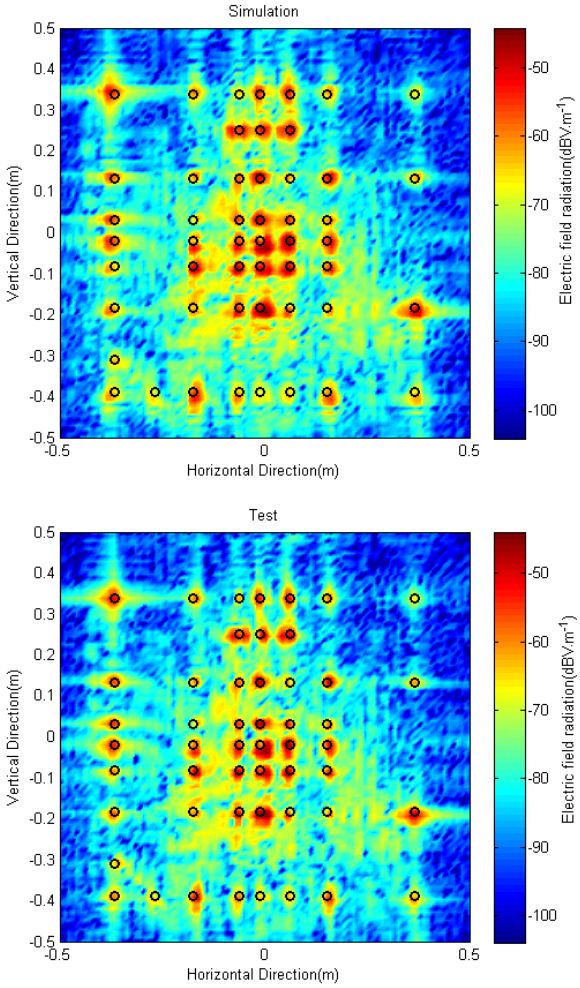

FIGURE 21. Imaging localization results at 20GHz.

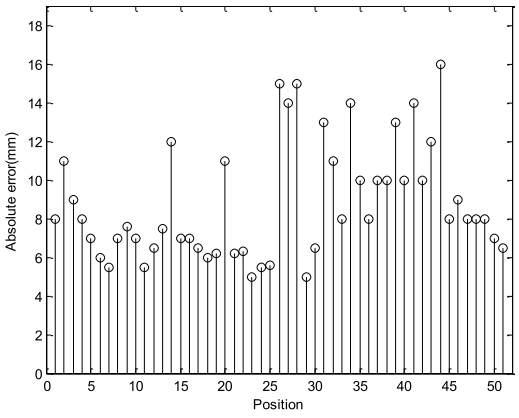

FIGURE 22. Localization error.

Of course, sparse sampling has a lower localization resolution than full sampling due to a lack of sufficient information. The positions of holes are mainly at the intersection of various lines. The resolution can be improved by increasing number of the sampling points. In practical engineering applications, the appropriate sampling method can be selected by comprehensively considering the testing cost and imaging resolution.

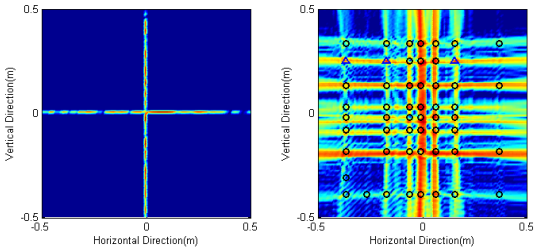

FIGURE 23. Sparse sampling localization analysis results.

VI. CONCLUSION

This paper investigates a method for locating electromagnetic radiation leakage based on synthetic aperture interferometric passive radiometer imaging. Electromagnetic radiation signals are measured at a certain distance from the spacecraft, forming visibility samples. The corrected brightness temperature of the target is obtained through the inverse Fourier transform, resulting in an image of the spacecraft surface's electromagnetic leakage localization. The effects of positional parameters, test antenna positioning accuracy, and scanning parameters on the imaging results were analyzed. A sparse sampling method based on particle swarm optimization is proposed to improve testing efficiency. Experiments were conducted on an electromagnetic leakage structure with a 1m×1m×1m cube and 51 holes on one face. The experiments verified that the algorithm of this paper can image and locate electromagnetic leakage points. Moreover, the method can perform imaging localization of electromagnetic leakage points at different frequencies. At specific frequencies, some holes may not cause severe electromagnetic leakage, and the method can identify them to avoid unnecessary shielding treatment. Additionally, the effectiveness of sparse sampling was verified through experiments, which can accurately locate electromagnetic leakage positions while saving 83.3% of the test time. The method of this paper can be applied to the localization of electromagnetic leakage sources in spacecraft with complex electromagnetic environments, offering significant application value for spacecraft shielding design.

DECLARATION OF COMPETING INTEREST

The authors declare that they have no known competing financial interests or personal relationships that could have appeared to influence the work reported in this paper.

REFERENCES

[1] G. Biancucci, A. Giordani, M. S. Sarto, E. Scione, and E. G. Ruà, "Graphene-based materials for radiated EMI control in satellite cavity," in *Proc. ESA Workshop Aerosp. EMC (Aerospace EMC)*, May 2022, pp. 1–6.
[2] B. Sun, W. Wang, K. Liang, and X. G. Xu, "Analysis method of electromagnetic compatibility for radio-frequency system between human spacecraft and adjoint satellite," *Chin. Space Sci. Technol.*, vol. 40, no. 2, pp. 49–53, Apr. 2020.
[3] K. O'Brien, "Spacecraft shielding for a Mars mission," *Adv. Space Res.*, vol. 36, no. 9, pp. 1731–1736, Jan. 2005.
[4] H. Daneshvar, K. G. Milan, A. Sadr, S. H. Sedighy, S. Malekie, and A. Mosayebi, "Multilayer radiation shield for satellite electronic components protection," *Sci. Rep.*, vol. 11, no. 1, p. 20657, Oct. 2021.

[5] L. Wang, Y. En, and Z. Zhu, "An ultrawideband differential magnetic-field probe for near-field scanning," *IEEE Microw. Wireless Technol. Lett.*, vol. 33, no. 2, pp. 224–227, Feb. 2023.
[6] Y. T. Zhang, M. Xiao, L. Zhang, H. A. Zhou, and Z. Lyu, "EMC performance evaluation of mobile communication satellites based on near-field scanning," *Syst. Eng. Electron.*, vol. 42, no. 9, pp. 1897–1902, Sep. 2020.
[7] J. Zhang, K. W. Kam, J. Min, V. V. Khilkevich, D. Pommerenke, and J. Fan, "An effective method of probe calibration in phase-resolved near-field scanning for EMI application," *IEEE Trans. Instrum. Meas.*, vol. 62, no. 3, pp. 648–658, Mar. 2013.
[8] J. Wen, X.-C. Wei, Y.-L. Zhang, and T.-H. Song, "Near-field prediction in complex environment based on phaseless scanned fields and machine learning," *IEEE Trans. Electromagn. Compat.*, vol. 63, no. 2, pp. 571–579, Apr. 2021.
[9] J. Meng, Y. X. Teo, D. W. P. Thomas, and C. Christopoulos, "Fast prediction of transmission line radiated emissions using the Hertzian dipole method and line-end discontinuity models," *IEEE Trans. Electromagn. Compat.*, vol. 56, no. 6, pp. 1295–1303, Dec. 2014.
[10] M. Sørensen, I. B. Bonev, O. Franek, and G. F. Pedersen, "Assessment of the Huygens' box method with different sources near obstacles," *IEEE Trans. Electromagn. Compat.*, vol. 62, no. 2, pp. 433–442, Apr. 2020.
[11] S. Xia, H. Wang, Y. Wang, Z. Wu, C. Hwang, and J. Fan, "Dipole-moment-based reciprocity for practical desensitization identification and mitigation," *IEEE Trans. Electromagn. Compat.*, vol. 65, no. 4, pp. 1017–1026, Aug. 2023.
[12] Q. Huang, L. Zhang, J. Rajagopalan, D. Pai, C. Chen, A. Gaikwad, C. Hwang, and J. Fan, "A novel RFI mitigation method using source rotation," *IEEE Trans. Electromagn. Compat.*, vol. 63, no. 1, pp. 11–18, Feb. 2021.
[13] S. Tao, H. Zhao, and Z. D. Chen, "An adaptive sampling strategy based on region growing for near-field-based imaging of radiation sources," *IEEE Access*, vol. 9, pp. 9550–9556, 2021.
[14] L. Wang, Y. Zhong, L. Chen, Z. He, J. Zhou, and Q. H. Liu, "Radiation diagnosis of PCBs and ICs using array probes and phaseless inverse source method with a joint regularization," *IEEE Trans. Microw. Theory Techn.*, vol. 70, no. 2, pp. 1442–1453, Feb. 2022.
[15] T.-H. Song, X.-C. Wei, J.-J. Ju, W.-T. Liang, and R. X. Gao, "An effective EMI source reconstruction method based on phaseless near-field and dynamic differential evolution," *IEEE Trans. Electromagn. Compat.*, vol. 64, no. 5, pp. 1506–1513, Oct. 2022.
[16] Q. Huang and J. Fan, "Machine learning based source reconstruction for RF desense," *IEEE Trans. Electromagn. Compat.*, vol. 60, no. 6, pp. 1640–1647, Dec. 2018.
[17] P. Li and L. J. Jiang, "Source reconstruction method-based radiated emission characterization for PCBs," *IEEE Trans. Electromagn. Compat.*, vol. 55, no. 5, pp. 933–940, Oct. 2013.
[18] J.-J. Ju, Z.-X. Xu, and X.-C. Wei, "EMI source positioning method based on phaseless near-field scanning," in *Proc. Asia–Pacific Int. Symp. Electromagn. Compat. (APEMC)*, Sep. 2022, pp. 813–815.
[19] Z. A. Wang, L. J. Jiang, J. F. Mao, and P. Li, "Numerical Green's function-based method for modeling radiated emission from PCBs in shielding enclosures," *IEEE Trans. Microw. Theory Techn.*, vol. 69, no. 12, pp. 5250–5258, Dec. 2021.
[20] Z. A. Wang, J. F. Mao, L. J. Jiang, and P. Li, "Localization and identification of EMI sources in shielding enclosures based on a two-step source reconstruction method," *IEEE Trans. Electromagn. Compat.*, vol. 65, no. 4, pp. 972–981, Aug. 2023.
[21] P. Maheshwari, H. Kajbaf, V. V. Khilkevich, and D. Pommerenke, "Emission source microscopy technique for EMI source localization," *IEEE Trans. Electromagn. Compat.*, vol. 58, no. 3, pp. 729–737, Jun. 2016.
[22] K. Konno, S. Asano, T. Umenai, and Q. Chen, "Diagnosis of array antennas using eigenmode currents and near-field data," *IEEE Trans. Antennas Propag.*, vol. 66, no. 11, pp. 5982–5989, Nov. 2018.
[23] W. Fan, Z. Chen, and W. J. R. Hoefer, "Source reconstruction from wideband and band-limited responses by FDTD time reversal and regularized least squares," *IEEE Trans. Microw. Theory Techn.*, vol. 65, no. 12, pp. 4785–4793, Dec. 2017.
[24] X. L. Dong, X. O. Xu, and X. Y. Xu, *Introduction to Microwave Remote Sensing*. Beijing, China: Science Press, 2014.
[25] H. Chen, H. Zhang, Z. Ni, and R. Li, "Research on imaging detection of RF leakage on the surface of spacecraft," in *Proc. Int. Symp. Electromagn. Compat.*, Sep. 2012, pp. 1–4.
[26] *Space Engineering—Electromagnetic Compatibility*, Standard ECSS-E-ST-20-07C, European Cooperation for Space Standardization, Noordwijk, The Netherlands, Jan. 2022.

YUTING ZHANG (Member, IEEE) received the Ph.D. degree from Harbin Engineering University, in 2011. He is currently a Senior Engineer with Beijing Institute of Spacecraft System Engineering.

SHUANGHONG ZHOU received the M.S. degree in science from Harbin Engineering University, in 2007. He is currently with the College of Mathematical Sciences, Harbin Engineering University. His research interests include numerical solutions to partial differential equations, electromagnetic computation, and signal processing.

MIAO XIAO received the M.S. degree in communications engineering from Beijing University of Posts and Telecommunications, in 2013. He is currently an Engineer with Beijing Institute of Spacecraft System Engineering.